SCIENTIFIC REPORTS

OPEN

A strong and deformable *in-situ* magnesium nanocomposite igniting above 1000 °C

Received: 27 November 2017
Accepted: 19 April 2018
Published online: 04 May 2018

Sravya Tekumalla[1], Yogesh Nandigam[2], Nitish Bibhanshu[3], Shabadi Rajashekara[4], Chen Yang[1], Satyam Suwas[3] & Manoj Gupta[1]

Magnesium has been trending of late in automobile, aerospace, defense, sports, electronic and biomedical sectors as it offers an advantage in light-weighting. In aluminum, titanium, and steel dominated aerospace and defense sectors, applications of Mg were banned/restricted until recently due to perceived easy ignition and inability to self-extinguish immediately. Strength is generally inversely related to ductility, weak texture and unrelated to ignition resistance, making it challenging to optimize all four concurrently in a material. We address this challenge by designing a low density (~1.76 g.cm^{-3}) *in-situ* Mg nanocomposite. It is a resultant of a sequence of *in-situ* reactions during melt processing and extrusion. The *in-situ* formed Y_2O_3 nanoparticles exhibit coherency with matrix and lead to development of large amount of elastic and plastic strain fields around them. These nanoparticles and secondary phases (Mg_2Ca and Mg_2Y) are responsible for the nanocomposite's high tensile strength (~343 MPa). A weak texture mediated tensile ductility of 30% and compressive failure strain of 44% is observed. Further, the ignition temperature increased to 1045 °C (near the boiling point of Mg) due to the formation of protective surficial oxide layers aided by the presence of insulating Y_2O_3 nanoparticles, rendering the nanocomposite outperform other traditional commercial Mg-based materials.

Reduction in weight of aircrafts and rockets in transportation sector accounts for a pronounced increase in the fuel efficiency and is an assertive route to restrict the emissions (emissions from transportation sector constituting up to 14% in 2010 & 26% in 2014)[1]. Replacement of the currently dominant aluminum, titanium alloys and steels will turn out to be a game changer in this field, primarily in view of the coarsening climate change. For decades now, research is being done on developing suitable light weight, high performance magnesium alloys[2,3]. However, we are not fully equipped with magnesium technology to suit the automobile, aviation and defense industries. The factors limiting the implementation of these materials are: (i) a limited toughness under static and dynamic loading due to a strong texture; (ii) high susceptibility to ignition (reason for Mg to be popular in pyro applications); and (iii) poor corrosion resistance.

Amongst these three limiting factors, the corrosive tendencies of magnesium alloys can be curbed by employing the coating technology[4] and by incorporating the right choice of alloying elements[5–7]. While the corrosive tendencies of magnesium alloys can be controlled to an extent, their high flammability continues to remain a problem. The fire extinguishers available today in commercial aircrafts cannot extinguish the fire caused due to the burning of Mg as Mg fire is highly reactive and intensifies over time[8]. It is commonly known that an increase in corrosion resistance occurs with a concurrent sacrifice of mechanical strength[9]. Although a similar relationship has not yet been certainly established for the ignition characteristics, like corrosion, it is also predominantly controlled by oxidative mechanisms. Besides, there is a dearth of Mg alloys that satisfy the criterion of mechanical suitability (strength and toughness) coupled with non-flammable characteristics; giving rise to a ban on the usage of Mg in aircrafts by Federal Aviation Administration (FAA)[10]. In 2014, the ban was lifted (except for the primary structure[11]) since Mg alloys like Elektron 43 and Elektron 21 satisfied the requirements of FAA[12]. However, since

[1]Department of Mechanical Engineering, National University of Singapore, 9 Engineering Drive 1, Singapore, 117576, Singapore. [2]Department of Metallurgical and Materials Engineering, Indian Institute of Technology Roorkee, Uttarakhand, 247667, India. [3]Department of Materials Engineering, Indian Institute of Science, Bangalore, 560012, India. [4]Laboratory of Physical Metallurgy and Materials Engineering, Unité Matériaux Et Transformations, UMR CNRS 8207, Université Lille – 1 Sciences et Technologies, 59650, Villeneuve d'Ascq, France. Correspondence and requests for materials should be addressed to S.T. (email: tvrlsravya@u.nus.edu) or M.G. (email: mpegm@nus.edu.sg)

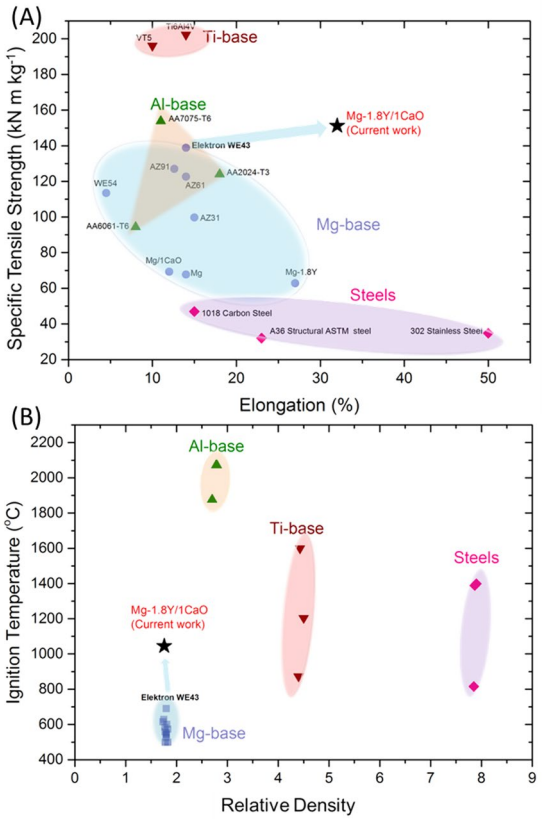

Figure 1. Holistic properties constituting specific strength-ductility-ignition temperature of the Mg-1.8Y/1CaO nanocomposite in comparison to the commercially available alloys. (**A**) Density normalized tensile yield strength versus elongation to failure of nanocomposite in the current work compared with commercially used alloys in aerospace applications; **(B)** An overview of the ignition properties and relative density of the commercial metallic materials. Ignition temperature versus relative density of commercial Mg-base alloys (AZ31, AZ91, Elektron WE43), commercial Al-base alloys (AA2024, AA6061 and AA7075), commercial Ti-base alloys (Ti6Al4V, VT5 alloy) and commercial steels (302 stainless steel, 1018 stainless steel, A36 structural steel).

very limited alloys satisfy this criterion, there is a large scope for developing suitable ignition and fire resistant magnesium based materials.

The governing mechanism of ignition of Mg alloys is very different as compared to the aircraft materials like Al alloys (AA7075) and Ti alloys (Ti6Al4V). Al and Ti develop protective surface layers and therefore show no sight of ignition until 2072 °C and 850 °C[13,14], respectively. In comparison, Mg has a poor Piling Bedworth ratio, forming non-adherent and non-protective surface layers which result in ignition in solid state, when the Mg vapor pressure is sufficient. To address this, several attempts in terms of modifying alloy chemistry and geometrical factors have been made, however, with limited attention paid to composites[15]. Composite materials[16,17], with their high specific stiffness and low coefficient of thermal expansion (CTE), provide the necessary characteristics to produce lightweight and dimensionally stable structures in aircraft and spacecraft missions. Nanocomposites of Mg base despite having a sound combination of mechanical and thermal stabilities[15,18], remained largely unexplored in the field of ignition resistant materials and the underlying mechanisms are unclear. By exploiting the thermodynamic feasibility of the reactions, hence forming nanoparticles *in-situ*, novel *in-situ* fabrication of magnesium based nanocomposites is designed. The *in-situ* Mg-1.8Y/1CaO (wt.%) nanocomposite, designed to overcome the limitations of poor strength, ductility, strong texture and ignition tendency, is synthesized using disintegrated melt deposition technique[17] and thermo-mechanically processed by extrusion at 350 °C. It is to be noted that the microstructure and properties reported henceforth are for the as-extruded materials.

Results and Discussion

Holistic outline of properties. Figure 1 shows the combination of properties exhibited by the extruded nanocomposite. It exhibits very high specific tensile yield strength (~152 kN.m.kg^{-1}), elastic modulus of 45 GPa and a large tensile elongation (~30%) at room temperature, as compared to commercial Mg alloys with specific strength of 60–130 kN.m.kg^{-1}. Consequently, the nanocomposite has an extremely high toughness (of 101 MJ/m^3 ~7 times higher than that of pure Mg)[19] which is an indicative of its promising bend-before-break ability. In the aerospace and defense sectors, materials are typically subjected to dynamic stresses and to be able to withstand loads without failing is imperative for Mg alloys in order to compete with the contemporary Al and Ti alloys. Under dynamic conditions, conventional Mg alloys usually fail at elongations less than 25%[20]. Before failure, the

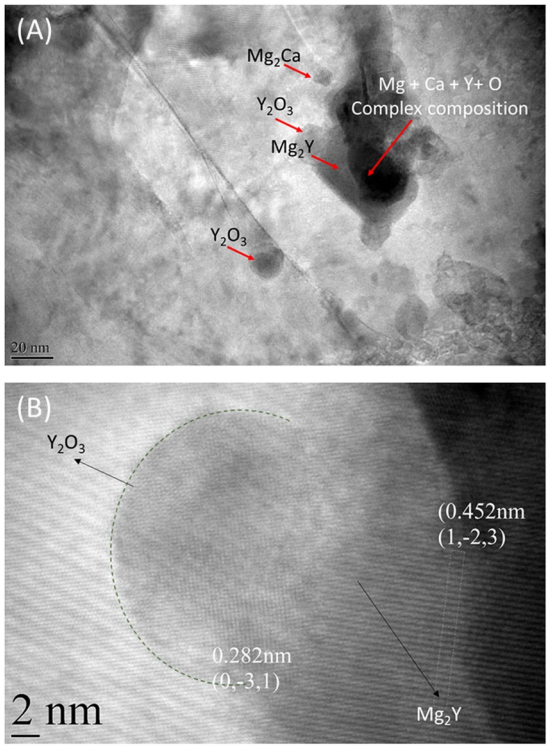

Figure 2. High-resolution transmission electron micrographs of the nanocomposite. (**A**) Distribution of phases and reinforcement in the matrix of the Mg-1.8Y/1CaO nanocomposite; and (**B**) a matrix-reinforcement interface showing the yttria nanoparticle emerging out of Mg_2Y phase.

Mg-1.8Y/1CaO has an excellent deformability under both static and dynamic compression withstanding strains up to 44% and 41% respectively. Figure 1A shows that the Mg-1.8Y/1CaO nanocomposite displays far superior mechanical performance in comparison with the FAA approved Elektron WE43 alloy[21] and conventionally used Mg, Al, Ti and Fe based commercial alloys[13,14,22–27], thus validating its unparalleled mechanical suitability.

Simultaneous existence of mechanical sturdiness and non-susceptibility to ignition is an important criterion, yet extremely challenging. Figure 1B, Fig. S6A and Table S1 show an ignition temperature of 1045 °C for Mg-1.8Y/1CaO nanocomposite, which is only marginally lower than the boiling point of magnesium (1091 °C). A holistic outline of the candidate materials[13,14,22–27] in terms of relative density and ignition temperature is given in Fig. 1B. Since the melting temperature of Mg is 650 °C, it is presumed that Mg auto-ignites at or below 650 °C. However, modification of the chemistry by incorporation of Y and CaO altered the reaction sequence at the surface of the nanocomposite when exposed to high temperatures, which is discussed in the subsequent sections.

***In-situ* evolution of a multi-component structure.** We used DSC and TEM to evaluate the microstructure and phases present in the nanocomposite. From the DSC curves (Fig. S3A), it is explicit that the nanocomposite undergoes transformation vis-a-vis both Mg-1.8Y and Mg/1CaO: indicating the presence of Mg-Y phase and Mg_2Ca phase (transformation at ~407 °C[28]). Through a detailed TEM evaluation (Figs 2A,B, S4A,B), the following are concluded:

(i) undiscernible clusters of Mg + Y + Ca + O (Fig. 2A) with complex compositions - result of a possibly incomplete transformation;
(ii) striking presence of spherical Y_2O_3 particles of the order of 15–20 nm length scale, an indication of an *in-situ* reaction sequence at the matrix-reinforcement interface (Fig. 2A and 2B);
(iii) a resultant of an incomplete reaction where the spherical Y_2O_3 emerge out of Mg_2Y phase (submicron − 1 micron size range) (Fig. 2B); and
(iv) a few CaO nanoparticles (40 nm) intact in the matrix (Fig. S4B) while a few reacting with the Mg-1.8Y matrix by dissolving to form barrel shaped Mg_2Ca of the order of 10–20 nm (Fig. S4B).

These results are consistent with the previous studies on Mg-CaO system where transformation of CaO to Mg-Ca phase occurs[28,29]. However, in the current work, due to the presence of Y in the matrix, formation of brittle MgO can be avoided. Instead, formation of Y_2O_3 (nano sized and spherical shaped) occurs as a consequence of higher reactivity of Y leading to *in-situ* reactions between matrix and reinforcement. Similar observations of reactions were observed in a ZnO introduced Mg-1.8Y alloy[30]. These *in-situ* formed stable nano Y_2O_3 and Mg_2Ca ascertain the mechanical and thermal behavior of the nanocomposite, as discussed in the subsequent sections.

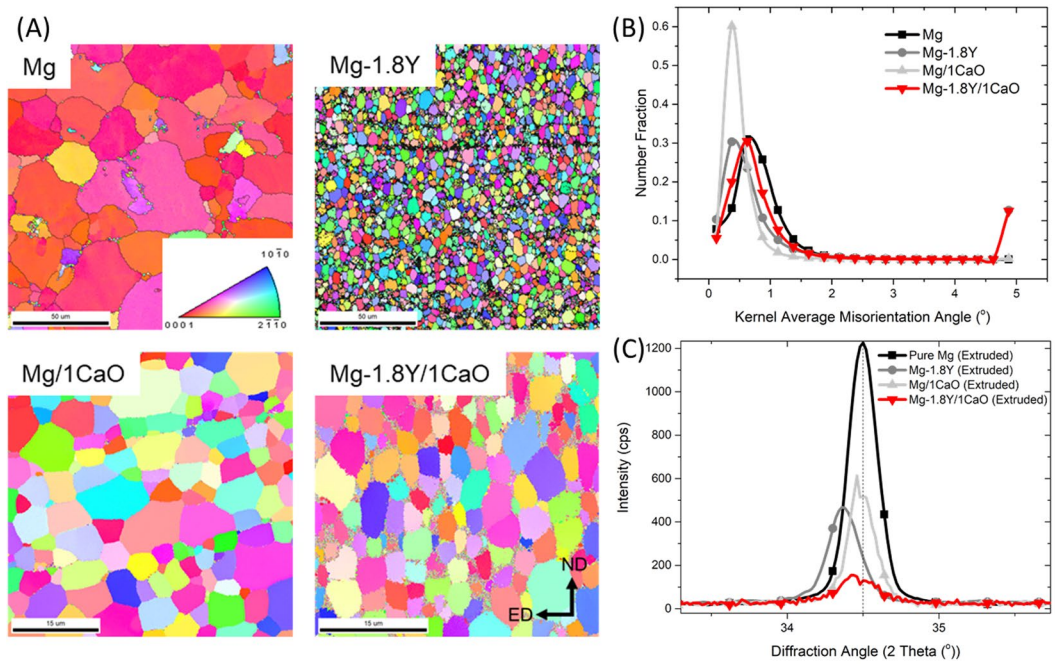

Figure 3. (**A**) Electron back-scattered diffraction patterns of the materials (**B**) Kernel Average Misorientation plots of the materials (**C**) X-ray diffraction results of the nanocomposite in comparison with its monolithic material. It must be noted that the difference in intensities correlated to the texture of the materials and is given in arbitrary units of counts per second.

Other key structural aspects like the final grain size and texture also are distinct in the nanocomposite in comparison to the monolithic materials. It is observed from EBSD Inverse pole figure maps (IPF) (Fig. 3A and Fig. S2) that the final grain size of Mg-1.8Y/1CaO is $6.3 \pm 0.9\,\mu m$ which is marginally higher than the average grain size of Mg-1.8Y ($5.4 \pm 0.6\,\mu m$), but lower than Mg/1CaO ($8.3 \pm 1.8\,\mu m$) and pure Mg ($22.7 \pm 9.8\,\mu m$). Unlike in pure Mg, the grains in Mg-1.8Y/1CaO seemed to be more equi-axed and along the axial direction of the extruded rod. The combined addition of Y and CaO in the matrix led to a decreased grain size as compared to Mg and Mg/1CaO. However, the reason for an increase in the grain size compared to the Mg-1.8Y alloy is thought to be the reaction sequence at the interface of matrix and reinforcement[31], resulting in less effect of grain refinement.

Further, all the materials are seen to have dynamically recrystallized microstructure. This can be affirmed through the kernel average misorientation (KAM) plots given in Fig. 3B. The greater extent to which the peak shifts towards the origin with an increased number fraction, the more the material is said to be recrystallized[32]. Since, the peaks for all the materials were at a misorientation angle lower than 1°, the materials can be considered to be recrystallized. From the IPF maps (Fig. 3A) and the inverse pole figures (Fig. S3B), it can be seen that Mg-1.8Y, Mg/1CaO and Mg-1.8Y/1CaO have relatively weaker textures as compared to the strong basal fiber in the texture of Mg (Typically, magnesium displays a strong extrusion texture which makes the material hard to deform along certain orientations). It is also ascertained that Mg-1.8Y/1CaO has the weakest texture (see intensities in Fig. S3B) in comparison to the other materials. Further, presence of a weak prismatic fiber is also seen in the nanocomposite, which is attributed to the effect of Y. This attribute results in exhibition of significantly high ductility by the nanocomposite[33] and renders the material suitable for applications involving extensive deformations.

Structural genesis of the mechanical properties. *In-situ* evolution of this multicomponent structure in the nanocomposite resulted in excellent properties. In magnesium alloys and nanocomposites, strengthening mechanisms like Hall-Petch strengthening are most commonly the reason to achieve higher yield strengths. The grain size of the nanocomposite is not significantly different from that of the alloy (Fig. S2), however the yield strength is more than double, an indication of dominance of strengthening mechanisms other than the Hall-Petch strengthening. Further, it is established that weaker textures in magnesium alloys (as obtained in this current study for the nanocomposite) result in lower yield strengths. However, the yield strength of the nanocomposite is very high. This is analysed to be due to the presence of the *in-situ* formed secondary phases as well as nanoparticles.

Y_2O_3 in the order of 15–20 nm length scale along the grain boundaries (Fig. S4A) interacts with grain boundaries, by acting as pinning sites and retards the dislocation motion. Further, there is a need to identify the internal strains induced in the nanocomposite due to the nanoparticles, to ascertain its high strength. The elastic component of the strain was analysed using XRD, while the plastic component was identified using KAM, which is an indirect measure of the geometrically necessary dislocations in the material. Addition of Y to Mg shifts the XRD peak at 34.5° to left (Fig. 3C), however with Y and CaO addition, the peak shifts to the right of the alloy and nearly coincides with that of Mg. This reveals that the nanocomposite has a higher elastic micro-strain as compared to

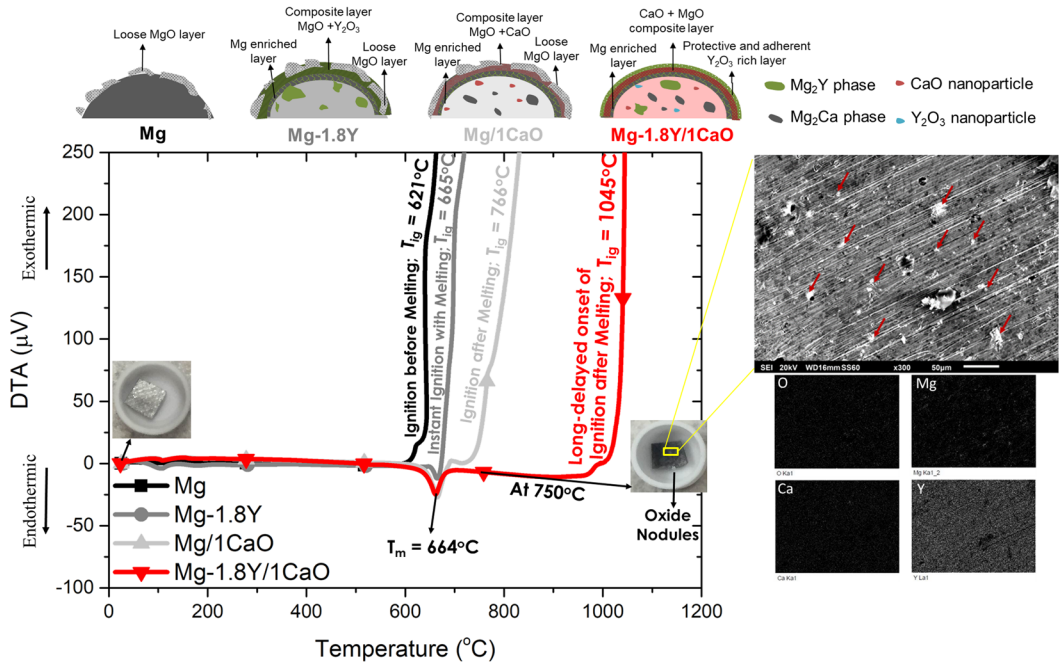

Figure 4. Schematic of DTA vs Temperature of all the materials. Endothermic peak indicates the melting temperature of the materials. Mg curve represents ignition before melting due to the presence of loose MgO layer; Mg-1.8Y alloy shows instant ignition with melting due to the presence of Y_2O_3 rich oxide scale; Mg/1CaO ignites after melting due to a more protective CaO + MgO scale and Mg-1.8Y/1CaO nanocomposite with the presence of multiple secondary phases and nanoparticles (not drawn to scale) developed *in-situ* develops a completely protective oxide layer that exhibits long-delayed onset of ignition. An inset of the sample heated until 750 °C in TGA and cooled down to room temperature shows an unignited Mg-1.8Y/1CaO. X ray mapping of the image indicates the dominating continuous presence of Y_2O_3 with a distributed presence of CaO and MgO layer on the surface indicating a Y_2O_3 rich surface.

that of the alloy. Further, from the KAM plot, it is also seen that Mg-1.8Y alloy and Mg/1CaO exhibit the least plastic micro-strain (shift in the peak to the left), while Mg and Mg-1.8Y/1CaO exhibit a higher micro-strain, which is mainly due to the recrystallization response of the materials as discussed in the previous section. The micro-strain results from KAM and the XRD data are an indicative of the presence of substantial elastic and plastic strains in the matrix in the nanocomposite. This is a result of the *in-situ* formation of nanoparticles, where the nanoparticles originate out of the phase through an exothermic reaction leaving a coherent interface as shown in Fig. 2B. In Y_2O_3 reinforced Mg nanocomposite reported by Goh *et al.*[34], an incoherent interface was observed, while this nanocomposite, with *in-situ* formed Y_2O_3, had a coherent interface with the matrix. This results in the substantial presence of strain fields around the nanoparticles, hence, an increase in the resistance to dislocation motion resulting in high yield strength. Thus, the *in-situ* formation of the nanoparticles contributed to an overall enhancement in its toughness and mechanical functioning.

Structural genesis of the ignition properties. The dominant mechanisms determining the ignition temperatures of magnesium based materials are complex and are not very well known, especially of the nanocomposites. The term 'ignition' is often misconstrued with terms like oxidation, melting, etc. The authors would like to clarify that ignition is the tendency of a material to burn instantly without being able to self-extinguish immediately. Materials like Al, despite having melting temperatures as low as 660 °C, have ignition temperatures greater than 2000 °C, i.e. Al does not burn instantly after melting due to formation of protective oxide layers. However, the same is not the case with traditional magnesium materials as they auto-ignite at temperatures lower than the melting temperatures (see Table S1), which is the reason for their non-applicability. For instance, pure Mg, as shown in Fig. 4, when subjected to slow heating in air, ignites completely at 621 °C even before melting (no melting/endothermic peak in curve corresponding to Mg). This is due to the high susceptibility of magnesium to oxidize at higher temperatures. The addition of yttrium lead to increased melting and ignition temperature of magnesium, leading to instant ignition with melting of the alloy at 665 °C. With addition of only CaO to Mg, the material ignited slightly after melting at 766 °C. In Mg-1.8Y/1CaO nanocomposite, a long-delayed onset of ignition occurred at 1045 °C despite the fact that the material had the same melting temperature as that of Mg-1.8Y and Mg/1CaO i.e. 664 °C. This is interesting, considering the fact that some Mg materials burn much before melting. This is a breakthrough in research for ignition resistant materials as this mechanism is akin to that of aluminum based materials. However, the two cannot be compared figuratively, as the boiling temperatures of Mg (1091 °C) and Al (2470 °C) are wide apart, thus leaving a huge disparity in the maximum ignition temperatures that can be achieved. This work achieved in getting very close to the boiling temperature of Mg by reaching ignition temperature of 1045 °C.

The detailed mechanism is discussed (see Fig. 4) as follows: when the bulk Mg-1.8Y/1CaO nanocomposite (with Mg_2Y, Mg_2Ca, CaO and Y_2O_3 dispersed in α-Mg matrix) is exposed to increasingly high temperatures, oxidation kinetics plays a dominant role. The preliminary oxide layer formation depends on the diffusion of the ions based on the diffusion coefficient data[35]. Mg^{2+} ions (smaller) diffuse faster than the Y^{3+} and Ca^{2+} ions (larger) and react with O^{2-} at the gas/metal interface leading to the formation of a thin outermost layer of MgO (Fig. 4). This causes an Mg-depleted zone underneath giving rise to an yttrium enriched layer (Fig. 4). Formation of yttrium rich oxide beneath MgO layer at the metal/oxide interface occurs until 390 °C (from the DSC results in Fig. S3A, the complete dissolution of phase occurs at 390 °C). As temperature increases, the dissolution of CaO to form Mg_2Ca occurs at 407 °C, leaving scope for the diffusion of Ca^{2+} ions as well through the layer at metal/oxide interface. Beneath these layers, another layer is feasible to form due to the faster diffusion of Ca^{2+} as compared to Y^{3+} on the nanocomposite surface with a complex composition of MgO, CaO and Y_2O_3 (Fig. 4). Thus formed dense composite oxide scale slows down the outward diffusion of Mg^{2+}. With increasing temperatures, the MgO layer loses its protective nature and breaks away leaving behind the Y_2O_3 rich layer. This stable layer prevents the exposure of Mg to oxygen resulting in slower increase in surface temperature.

Based on the SEM results (Fig. 4) of the surface analysis of sample heated until 750 °C, Y_2O_3 rich layer is stable until a much higher temperature as compared to MgO and at 750 °C. In addition, the surface of the nanocomposite indicated presence of localized oxide nodules of MgO (Fig. 4), some visible to the eye. When the temperature increases further, the surface layer becomes loose leading to further exposure of these nodules to the air. Due to the exothermic nature of the oxidation process, the high localized heat energy released causes evaporation of Mg, when these Mg vapors come in contact with air, ignition of the nanocomposite occurs. Alongside the surface oxide layers of Y_2O_3, the *in-situ* evolved thermally stable Y_2O_3 nanoparticles (insulators) delay the onset of ignition by not allowing the heat transfer to take place in the matrix across the nanoparticles. Though the modification of alloy chemistry cannot prevent the complete ignition of the material, it delays the onset of ignition until close to its boiling temperature. Further elaborate discussion in comparison to the monolithic alloys is given in the Supplementary material.

Multitudinous functions of yttrium. Yttrium plays a multitudinous role in the excellent functioning of the nanocomposite. Firstly, it assists in the reduction of CaO into the matrix. From the Ellingham diagram (free energy versus temperature plots), it can be seen (Fig. S8) that the line of $2Y + 3O \rightarrow Y_2O_3$ is under the $Ca + O \rightarrow CaO$ line at 750 °C (melting temperature) (however, the two lines are close at that temperature). This could possibly be the reason for partial reduction of CaO as the kinetics also plays a crucial role. Very few other elements like Tm (Thulium) satisfy this criterion (Fig. S8). This helps in the dissolution of CaO and preferential oxidation of Y to form Y_2O_3. These Y_2O_3 particles enhance the ignition temperature and strength in the nanocomposite by providing a non-conductive interface for heat transfer as well as by being hard obstacles for dislocation motion. Secondly, Y promotes activity of non-basal slip as shown in Figs 3A and S3B and established previously[36]. This results in the excellent deformability of Mg under both static and dynamic conditions[37]. Thirdly, it aids in the modification of the surficial oxide layer. The formation of a dense compact oxide layer of Y_2O_3 (mainly), CaO and MgO is possible due to the addition of Y and its synergistic effect with Ca to form a stable oxide layer[38]. Each or two of the afore mentioned roles may be displayed by other alloying elements as well, however, the collective role of all the three functions can be displayed by only Y, thus making the designed composition, for the nanocomposite, unique.

Competition with commercial structural materials. The nanocomposite with such superior properties is fabricated by a fairly simple process of casting and extrusion, similar to that of the Al and Ti alloys. The novel *in-situ* reactions taking place during the processing aid in uniform and homogeneous dispersion of nanoparticles in magnesium matrix, which otherwise is not possible in traditional Mg nanocomposites fabricated using conventional routes. Thus, the *in-situ* nanocomposites of Mg render the processing industrially viable using standard routes of processing. Plots of ignition temperature versus specific strengths in various commercial alloys are shown in Fig. 5. The present Mg-1.8Y/1CaO nanocomposite possesses a relative density of 1.76 and its specific strength is much higher than that of steels and most Mg alloys and Al alloys, while its deformability is at par with/exceeding Al, Ti base alloys and steels. Its ignition temperature (1045 °C) is only slightly lower than the boiling temperature and is much higher than FAA approved Elektron WE43 alloy (690 °C) and comparable to that of Ti base alloys and steels and lower than Al base alloys. It is almost practically impossible to raise the ignition temperature of Mg alloys/nanocomposites beyond the boiling temperature. It may be noted that Mg suffers from a poor boiling temperature of 1091 °C, while Al and Ti boil at 2470 °C and 3287 °C, hence reaching high ignition temperatures like that of Al is impracticable. This lightweight, high strength, ductile, 100% recyclable and ignition resistant nanocomposite has a great potential in defense and aerospace applications, and can be extended to others including automotive, electronic, sporting and biomedical applications. Further, employing this particular material combination can also help prevent the usage of environmentally unfriendly cover gases during material fabrication as the nanocomposite develops a very stable dense protective layer that can inhibit the initiation of fire even during melting[39].

Conclusions

In short, an *in-situ* Mg-1.8Y/1CaO nanocomposite with superior mechanical (tensile strength ~343 MPa, ductility ~30%) and ignition temperature (1045 °C) has been reported for the first time. A thermodynamically reactive matrix with Y as an alloying element to Mg is chosen such that it aids in the *in-situ* reaction as well as imparts ductility to the matrix by weakening texture. The CaO reinforcement reacts with the Mg-1.8Y matrix at processing temperatures to form *in-situ* Mg_2Ca and *in-situ* Y_2O_3 nanoparticles with a coherent interface with the matrix. Despite a weak texture, due to the presence of substantial elastic and plastic strain fields around the nanoparticles,

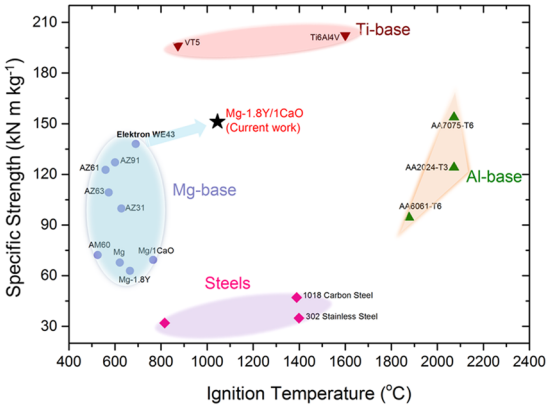

Figure 5. Density normalized tensile strength versus ignition temperature of Mg-1.8Y/1CaO in comparison with the commercial Mg-base alloys, Al-base alloys, Ti-base alloys and steels.

the nanocomposite exhibited high strengths. Further, the presence of thermally insulating Y_2O_3 nanoparticles and formation of surficial complex oxide layers delayed the onset of ignition until 1045 °C.

This finding is a breakthrough for the budding magnesium composite technology and broaches a potential for the progress in research towards magnesium based nanocomposites in the interest of light-weighting and suggests industrially scalable new *in-situ* synthesis of nanocomposites.

Methods

Primary processing. Mg-1.8Y/1CaO (wt.%) nanocomposite was synthesized by melting and casting commercially pure Mg turnings (99.9% purity; supplied by Acros Organics, USA), Mg-30% (wt.%) Y master alloy (99% purity; supplied by Sunrelier Metal Co. Limited, China) and CaO nanoparticles (Nanoshel LLC, USA; 40 nm average size). The synthesis technique employed is the DMD (Disintegrated Melt Deposition) method[17]. This method involves adding the raw material (i.e. Mg, Mg-30Y and CaO) in alternate layers to form a sandwich pattern in a graphite crucible and heating it in an electrical resistance furnace to 750 °C in a protective inert argon gas atmosphere. This method employs a combination of vortex stirring of melt at 450 rpm for 5 minutes. The stirrer used was a mild steel impeller with twin blade (pitch 45°) coated with Zirtex 25 (86% ZrO_2, 8.8% Y_2O_3, 3.6% SiO_2, 1.2% K_2O and Na_2O, with 0.3% trace inorganic) in order to avoid contamination of molten metal with iron. The melt, released through an orifice of 10 mm diameter, located at the crucible's base was disintegrated by two argon gas jets that were oriented normal to the melt stream to obtain near equi-axed grain structure. The disintegrated melt was then deposited on the substrate forming an ingot of 40 mm diameter.

Secondary processing. Billets (length: 45 mm and diameter: 36 mm) of Mg-1.8Y/1CaO nanocomposite obtained from DMD technique were homogenized at 400 °C for 1 hour and extruded at 350 °C to obtain rods of 8 mm diameter, hence maintaining an extrusion ratio of 20.25:1. Samples were taken from these rods for further analysis.

Grain size measurement. Grain size of each material was obtained using the linear intercept method following the ASTM E112–13 standard using images from an optical microscope (Olympus) on polished and etched samples (etchant: 60 ml ethylene glycol, 20 ml acetic acid, 1 ml nitric acid and 20 ml distilled water).

X Ray Diffraction. An automated Shimadzu LAB-XRD-6000 (Cu Kα; λ = 1.54 A°) spectrometer with a scan speed of 2°/min was used for X-ray diffraction analysis of samples. Macro textures were measured using a Bruker D8-Discover texture goniometer using Co-Kα radiation. During X-ray texture measurements all the samples were irradiated perpendicular to the extrusion direction along the radial plane. Six pole figures viz., (1 0 1 0), (0 0 0 2), $(1\,\bar{0}\,1\,1)$, $(1\,\bar{0}\,1\,2)$, $(1\,\bar{1}\,2\,0)$ and $(1\,\bar{1}\,2\,\bar{2})$ were measured and orientation deformation functions (ODFs) were calculated using ADC algorithm using a Labotex Software. Inverse pole figures were calculated from the ODFs.

Phase/reinforcement determination. Phase analysis was performed using scanning electron microscopes (JEOL JSM-6010 and Hitachi FESEM-S4300) coupled with energy dispersive spectrometric analysis (EDS) and a 200 kV Tecnai F20 Transmission Electron Microscope (TEM) on polished and etched samples. Slices of 200 µm were taken from each material, thinned mechanically to 50 µm, made electron transparent in a Gatan polisher and a Precision Ion Polishing System (PIPS) with voltage of 3.5 keV and a tilt angle of 7°.

Micro-texture. Micro-texture of the extruded rods was obtained using the electron back-scatter diffraction (EBSD) technique in a Field Emission Gun Scanning Electron Microscope (FEG-SEM) by FEI Company. The samples were cloth polished with diamond paste (0.05 microns) to obtain a mirror finish, with kerosene acting as a lubricant. Further, mechanical electro-polishing was carried out (using an electrolyte containing 3:5 solution of H_3PO_4 in ethanol and pure aluminum cathode at 3 V for 30 s and 1.5 V for 3 min at ~0 °C) in the final polishing step. The EBSD scans were recorded on the radial plane of the samples parallel to the extrusion direction (ED). Kernel average misorientation (KAM) of each EBSD spot with all of its neighbouring spots was calculated with

the provision that misorientations exceeding 5° were excluded from the average calculation. The misorientation between a grain at the centre of the kernel and all points at the perimeter of the kernel were measured. The local misorientation value assigned to the centre point was the average of these misorientations, which could be obtained from the EBSD scans. Maps, constructed using this method, are helpful in visualizing the distribution of local misorientation within a grain.

Phase transformation determination. DSC reaction studies using Shimadzu DSC - 60 instrument was carried out at a heating rate of 5 °C/min from room temperature to 600 °C in flowing argon atmosphere to determine the phase transformations in the alloy and nanocomposites. The deflection in the curves (upward peak or downward peak) indicates the occurrence of reactions due to phase transformations.

Ignition testing. The ignition temperatures were determined using a simultaneous Thermo Gravimetric Analyzer (TGA)- Differential Thermal Analyzer (DTA). Samples of dimensions $2 \times 2 \times 1\,mm^3$ were heated from 30 °C to 750 °C and 30 °C to 1200 °C with a heating rate of 30 °C/min each in purified air with a flow rate of 50 ml/min. The point at which a rapid increase in the weight of the sample is triggered (as a result of sharp oxidation upon ignition) is considered as the ignition temperature[15]. After the sample was burnt out, the temperature rate was restored to the initial set-value. The crucible was removed immediately after the test, cooled sufficiently in order to avoid contamination of TGA and overflow of the ignited powder from the sample. For each composition, 3 tests were performed to ensure consistency in the results.

Elastic Modulus Determination. The elastic modulus of the nanocomposite was measured using the resonance frequency damping analyzer (RFDA) equipment from IMCE, Belgium. In this method, the material is manually impulse excited at room temperature. The RFDA basic system measures the resonant frequencies and internal friction or damping of samples and calculates the Young's modulus according to the ASTM E1876–15 standard. The vibration signal of the material (7 mm diameter, 40 mm length) is recorded and the elastic properties are calculated by the dedicated RFDA basic software.

Tensile testing. A fully automated servo-hydraulic Model MTS 810 mechanical testing machine was used to determine the tensile behavior of the developed Mg alloys, conforming to ASTM test method E8/E8M-13a. Specimen with a diameter of 5 mm and gauge length of 25 mm were used for the tensile tests and were tested at a strain rate of $1.6 \times 10^{-4}\,s^{-1}$. A clip-on type extensometer of Instron 2630e100 series was used to determine the displacement/strain. Five tests were performed on each sample to ensure consistency and the representative result is taken in this work.

Quasi-static compressive testing. Quasi-static compression tests were performed on a fully automated servo-hydraulic mechanical testing machine, Model-MTS 810 conforming to ASTM test method E9-09. Specimen of 7 mm diameter and 7 mm length were tested at a strain rate of $1.6 \times 10^{-4}\,s^{-1}$. For each composition, 5 tests were performed to ensure consistency in the results. Five tests were performed on each sample to ensure consistency and the representative result is taken in this work.

Dynamic compressive testing. High-strain-rate compression tests were performed using a Split Hopkinson Pressure Bar (SHPB) at ambient temperature (298 K). In the SHPB setup used in this study, the specimen is sandwiched between the incident bar and the transmission steel bar. The contact end of the specimen/pressure bar was covered with a silicone grease to minimize friction. A high-pressure chamber was used to launch a striker bar, which impacts one end of the incident bar and generates an elastic wave pulse. Strain gauges were bonded on the surface of the incident and transmission bars to detect the propagation of stress waves. Because the stress equilibrium in the specimen was confirmed by the measured stress waves, one wave analysis was conducted in this study. Strain rate $\dot{\varepsilon}(t)$, stress $\sigma(t)$, and strain $\varepsilon(t)$ were calculated using the following equations[40].

$$\dot{\varepsilon}(t) = -\frac{2C_B\varepsilon_B(t)}{L_0};\ \varepsilon(t) = -\frac{2C_B}{L_0}\int_0^t \varepsilon_R(t)dt;\ \sigma(t) = \frac{E_B A_B \varepsilon_T(t)}{A_0}$$

where C_B, E_B and A_B are the elastic wave speed, elastic modulus and cross-sectional area of the bars, respectively; L_0 and A_0 are the length and cross-sectional area of the specimen; ε_R is the reflected strain, ε_T is the transmitted strain, and $\dot{\varepsilon}$ is the strain rate. The average strain rate was measured to be $1.4 \times 10^3\,s^{-1}$ for a specimen of 5.0 mm height. For each composition, 5 tests were performed to ensure consistency in the results.

Data Availability Statement. All data generated or analysed during this study are included in this published article (and the Supplementary Information files).

References

1. Inventory of U. S. Greenhouse Gas Emissions and Sinks: 1990–2014. In: *Environmental Protection Agency* (ed^(eds) (April, 2016).
2. Tekumalla, S., Seetharaman, S., Almajid, A. & Gupta, M. Mechanical Properties of Magnesium-Rare Earth Alloy Systems: A Review. *Metals* **5**, 1 (2015).
3. Stoudt, M. R. Magnesium: Applications and advanced processing in the automotive industry. *JOM* **60**, 56–56 (2008).
4. Gray, J. & Luan, B. Protective coatings on magnesium and its alloys—a critical review. *Journal of alloys and compounds* **336**, 88–113 (2002).
5. Atrens, A., Song, G.-L., Liu, M., Shi, Z., Cao, F. & Dargusch, M. S. Review of Recent Developments in the Field of Magnesium Corrosion. *Advanced Engineering Materials* **17**, 400–453 (2015).
6. Song, G. & Atrens, A. Understanding Magnesium Corrosion—A Framework for Improved Alloy Performance. *Advanced Engineering Materials* **5**, 837–858 (2003).

7. Song, G. L. & Atrens, A. Corrosion Mechanisms of Magnesium Alloys. *Advanced Engineering Materials* **1**, 11–33 (1999).
8. Czerwinski, F. Controlling the ignition and flammability of magnesium for aerospace applications. *Corrosion Science* **86**, 1–16 (2014).
9. Xu, W. *et al*. A high-specific-strength and corrosion-resistant magnesium alloy. *Nat Mater* **14**, 1229–1235 (2015).
10. Marker, T. R. Development of a Laboratory Scale Flammability Test for Magnesium Alloys Used in Aircraft Seat Construction. (ed^(eds William, Hughes J). Federal Aviation Administration Technical Center (2014).
11. Lyon, B. G. a. P. Magnesium Alloys in Aerospace Applications, Past Concerns, Current Solutions. In: *Triennial International Aircraft Fire & Cabin Safety Research Conference* (ed^(eds) (2007).
12. Elektron, M. (ed^(eds). Magnesium Elektron (2016).
13. Thomas, R., Strobridge, J. C. M., Alan, F. Clark Titanium combustion in turbine engines. (ed^(eds). Systems Research & Development Service, Federal Aviation Administration, U.S. Department of Transportation (1979).
14. Nguyen, K. & Branch, M. C. Ignition Temperature of Bulk 6061 Aluminum, 302 Stainless Steel and 1018 Carbon Steel in Oxygen. *Combustion Science and Technology* **53**, 277–288 (1987).
15. Tekumalla, S. & Gupta, M. An insight into ignition factors and mechanisms of magnesium based materials: A review. *Materials & Design* **113**, 84–98 (2017).
16. Chen, Y., Tekumalla, S., Guo, Y. B. & Gupta, M. Introducing Mg-4Zn-3Gd-1Ca/ZnO nanocomposite with compressive strengths matching/exceeding that of mild steel. *Scientific Reports* **6**, 32395 (2016).
17. Gupta, M, Wong, W. L. E. Magnesium-Based Nanocomposites: Lightweight Materials of the Future. *Materials Characterization* (2015).
18. Gupta, M. & Wong, W. L. E. Magnesium-based nanocomposites: Lightweight materials of the future. *Materials Characterization* **105**, 30–46 (2015).
19. Tekumalla, S. *et al*. Influence of Cerium on the Deformation and Corrosion of Magnesium. *Journal of Engineering Materials and Technology* **138**, 031011-031011-031010 (2016).
20. Tekumalla, S. *et al*. Enhancing overall static/dynamic/damping/ignition response of magnesium through the addition of lower amounts (<2%) of yttrium. *Journal of Alloys and Compounds* **689**, 350–358 (2016).
21. Magnesium Elektron WE43 Alloy (UNS M18430). (ed^(eds) (2013).
22. Czerwinski, F. *Magnesium Injection Molding*. Springer US (2007).
23. Bettles, C., Barnett, M. *Advances in Wrought Magnesium Alloys: Fundamentals of Processing, Properties and Applications*. Elsevier Science (2012).
24. Jayalakshmi, S., Gupta, M. *Metallic Amorphous Alloy Reinforcements in Light Metal Matrices*. Springer International Publishing (2015).
25. Lyon, B. G. P. Magnesium Alloys in Aerospace Applications, Past concertns, Current solutions. In: *Triennial International Aircraft Fire & Cabin Safety Research Conference* (ed^(eds) (2007).
26. Kaufman, J. G. *Properties of Aluminum Alloys: Tensile, Creep, and Fatigue Data at High and Low Temperatures*. ASM International (1999).
27. Titanium Industries I. Material Safety Data Sheet For Titanium Metal (2011).
28. Wiese, B. *et al*. CaO dissolution during melting and solidification of a Mg–10 wt.% CaO alloy detected with *in situ* synchrotron radiation diffraction. *Journal of Alloys and Compounds* **618**, 64–66 (2015).
29. Jeong, J. *et al*. Transmission electron microscopy and thermodynamic studies of CaO-added AZ31 Mg alloys. *Acta Materialia* **61**, 3267–3277 (2013).
30. Tekumalla, S., Shabadi, R., Yang, C., Seetharaman, S. & Gupta, M. Strengthening due to the *in-situ* evolution of ß1′ Mg-Zn rich phase in a ZnO nanoparticles introduced Mg-Y alloy. *Scripta Materialia* **133**, 29–32 (2017).
31. Lu, L., Lai, M. O. & Chen, F. L. Al-4 wt% Cu Composite reinforced with *in-situ* TiB2 particles. *Acta Materialia* **45**, 4297–4309 (1997).
32. Biswas, S., Suwas, S., Sikand, R. & Gupta, A. K. Analysis of texture evolution in pure magnesium and the magnesium alloy AM30 during rod and tube extrusion. *Materials Science and Engineering: A* **528**, 3722–3729 (2011).
33. Sabat, R. K., Mishra, R. K., Sachdev, A. K. & Suwas, S. The deciding role of texture on ductility in a Ce containing Mg alloy. *Materials Letters* **153**, 158–161 (2015).
34. Goh, C. S., Wei, J., Lee, L. C. & Gupta, M. Properties and deformation behaviour of Mg–Y2O3 nanocomposites. *Acta Materialia* **55**, 5115–5121 (2007).
35. Aydin, D. S., Bayindir, Z., Hoseini, M. & Pekguleryuz, M. O. The high temperature oxidation and ignition behavior of Mg–Nd alloys part I: The oxidation of dilute alloys. *Journal of Alloys and Compounds* **569**, 35–44 (2013).
36. Sandlöbes, S., Zaefferer, S., Schestakow, I., Yi, S. & Gonzalez-Martinez, R. On the role of non-basal deformation mechanisms for the ductility of Mg and Mg–Y alloys. *Acta Materialia* **59**, 429–439 (2011).
37. Nagao, M., Terada, T., Somekawa, H., Singh, A. & Mukai, T. Deformation Behavior of Binary Mg-Y Alloy Under Dynamic Compression Loading. *JOM* **66**, 305–311 (2014).
38. Lee, T.-W. *et al*. Microstructural evaluation of oxide layers in CaO-added Mg alloys. *Journal of Alloys and Compounds* **635**, 5–10 (2015).
39. Kim, S. K., Lee, J.-K., Yoon, Y.-O. & Jo, H.-H. Development of AZ31 Mg alloy wrought process route without protective gas. *Journal of Materials Processing Technology* **187–188**, 757–760 (2007).
40. Chen, Y., Guo, Y. B., Gupta, M. & Shim, V. P. W. A study of the dynamic compressive response of AZ31/Al2O3 nanocomposites and the influence of nanoparticles. *International Journal of Impact Engineering* **89**, 114–123 (2016).

Acknowledgements

The authors gratefully acknowledge Ministry of Education Academic Research Funding (WBS# R-265-000-498-112) for the financial support in carrying out the experiment. The authors thank Mr. Juraimi for the help with extrusion and Mr. Hong Wei for the assistance with TGA. ST sincerely thanks NUS research scholarship for supporting her graduate program. SR sincerely acknowledges the Microscopy center in Institut Chevreul. The TEM facility in Lille (France) is supported by the Conseil Regional du Nord-Pas de Calais, and the European Regional Development Fund (ERDF).

Author Contributions

S.T. and Y.N. carried out the fabrication, testing of the nanocomposites, including analyses using SEM, XRD, TGA, DTA and DSC and the mechanical property analyses. S.T., N.B. and S.S. carried out and analysed the macro and micro texture of the materials using XRD and EBSD tools. S.R. carried out the TEM investigations and S.T., C.Y. and S.R. carried out the microstructural analysis. S.T. and M.G. designed the experimental program and S.T. coordinated, executed and interpreted the overall project and drafted the manuscript. All authors contributed to the analysis of the results and editing of the paper.

Additional Information

Supplementary information accompanies this paper at https://doi.org/10.1038/s41598-018-25527-0.

Competing Interests: The authors declare no competing interests.

Publisher's note: Springer Nature remains neutral with regard to jurisdictional claims in published maps and institutional affiliations.